

Selectivity- and Activity-Aware Catalyst Descriptors for CO₂ Hydrogenation on Alloy Nanocatalysts using Machine-Learned Force Fields

Prajwal Pisal,^{†,‡,¶,§} Ondrej Krejci,^{||,‡,⊥} and Patrick Rinke^{*,†,‡,¶,§}

[†]*Department of Physics, Technical University of Munich, James-Franck-Strasse 1, 85748 Garching, Germany.*

[‡]*Department of Applied Physics, Aalto University, P.O. Box 11000, AALTO, FI-00076, Finland.*

[¶]*Munich Center for Machine Learning, Germany.*

[§]*Atomistic Modeling Center, Munich Data Science Institute, Technical University of Munich, Walther-von-Dyck Str. 10, 85748 Garching, Germany*

^{||}*Department of Chemistry and Materials Science, Aalto University, P.O. Box 11000, AALTO, FI-00076, Finland.*

[⊥]*Department of Mechanical and Materials Engineering, University of Turku, Vesilinnantie 5, Turku, FI-20014, Finland.*

E-mail: patrick.rinke@tum.de

Abstract

Adsorption energy distributions (AEDs) have emerged as a powerful and increasingly adopted descriptor for catalytic performance in high-entropy alloys and, more

recently, in conventional metallic alloy nanocrystal catalysts. By accounting for diverse adsorption sites and crystallographic facets, AEDs more fully represent nanoparticle-based catalytic surfaces and show strong promise for accelerating rational design and discovery of heterogeneous catalysts, especially for CO₂ hydrogenation. However, previous approaches have not sufficiently resolved facet-specific contributions, despite the catalytic significance and prevalence of certain Miller planes in nanoscale catalysts, limiting their applicability in predicting activity and selectivity. Here, we introduce an updated facet-resolved framework for predicting catalytic activity, which also enables insight into selectivity toward C1 products. Universal machine-learned force fields trained on Open Catalyst Project data were employed to compute adsorption energetics across 226 experimentally observed metals, binary alloys, and ternary alloys, encompassing 1.4 million adsorption sites on 2,626 crystallographically distinct surfaces. Using statistical and unsupervised learning techniques, we analyzed facet-specific AEDs to identify highly active and methanol-selective facets. Our approach provides insight into the relationship between structure and catalytic performance metrics like activity and selectivity, and presents a set of alloy compositions and their respective surface orientations for experimental validation toward highly selective CO₂ hydrogenation.

Introduction

Sustainable conversion of sequestered carbon dioxide into methanol over heterogeneous catalysts is a key route toward carbon-neutral chemicals and demands predictive, scalable catalyst design strategies. Three principal catalytic pathways are pursued for CO₂ hydrogenation: thermal catalysis, electrocatalysis, and photocatalysis.¹ Among these, thermal catalysis is currently closest to industrial adaptation due to its technological maturity and compatibility with established large-scale hydrogenation processes.² Thermal CO₂ hydrogenation can, in principle, yield a range of valuable C1 products, including formic acid (HCOOH), methane (CH₄), and methanol (CH₃OH).³⁻⁵ In particular, methanol has attracted attention due to its

high energy density, versatility as a chemical feedstock, and compatibility with existing industrial infrastructure.^{3,4} However, developing efficient solid-phase catalysts for the thermal CO₂ hydrogenation requires simultaneous optimization of catalytic activity, long-term stability under reaction conditions, and selectivity toward the desired product. The synthesis of methanol-producing catalysts has been deeply influenced by similar processes, particularly syngas conversion. It has been established that the most efficient catalysts consist of metal, alloy, or oxide nanoparticles supported on porous oxide substrates, with metal and alloy nanoparticles playing the most pivotal role.^{6,7} However, exploration of their design space, comprising diverse facets and active sites, makes purely experimental screening prohibitively expensive and necessitates scalable computational approaches to guide catalyst discovery.^{8,9}

Theoretical and computational approaches provide a cost-effective route to guide experimental catalyst screening.¹⁰ Direct evaluation of catalytic activity via reaction barrier calculations remains computationally expensive, even for selected adsorption facets and sites. As a result, many studies rely on simplified descriptors that serve as proxies for catalytic activity. Most commonly, these include adsorption energies obtained from density functional theory (DFT)¹¹ or more reduced electronic descriptors such as the *d*-band center.^{12,13} However, single-site descriptors often neglect the site- and facet-heterogeneity inherent to nanoparticle catalysts, limiting their ability to capture activity and selectivity trends across complex alloy surfaces.¹⁴ Thus, developing representations that capture the physicochemical complexity of real catalytic systems is essential for rational catalyst design. Recent advances in data-driven approaches¹⁵ and machine-learned force fields (MLFFs)^{16–19} enable efficient sampling of large adsorption configuration spaces required to construct high-fidelity descriptors for realistic nanoparticle models.

In our previous work, we employed MLFFs^{18,20} to construct adsorption energy distributions (AEDs). AEDs are reaction-specific material descriptors that capture the adsorption landscape of key reaction intermediates across binding sites on nanocrystal facets. We demonstrated their utility in screening catalyst candidates for CO₂-to-methanol conversion.²¹

By capturing distributions rather than single adsorption energies, AEDs provide a compact statistical fingerprint for quantitative comparison of adsorption energetics and, thus, inferred catalytic performance across diverse materials.

While AEDs naturally account for multiple adsorption sites and, for nanocrystals, multiple facets, they are formulated as material-level descriptors. In this aggregated form, they do not explicitly resolve how individual facets contribute to the overall adsorption landscape. The aggregation of adsorption energies across all sampled sites effectively treats each site as equally representative, regardless of facet abundance or intrinsic activity, even though catalytic behavior is often dominated by a subset of low-index facets.²²

Motivated by the demonstrated success of AED-type descriptors in encompassing surface heterogeneity in high-entropy alloys,^{23,24} we hypothesize that the rich energetic information encoded in AEDs can be leveraged with more advanced statistical analyses to provide improved estimates of catalytic activity and selectivity. Previous studies have established such systematic correlation between adsorption energies of key intermediates and selectivity toward C1 products,^{22,24–26} further supporting our hypothesis.

Therefore, in this work, we aim to extend our previously developed MLFF-driven screening framework²¹ by applying AED-based analysis to experimentally relevant ternary alloy catalysts, thereby expanding the explored compositional space beyond pure metals and binary systems. As we intend to move beyond the collective description of all Miller facets, we adopt a facet-resolved AED framework that enables direct comparison of AEDs for individual facets without imposing *a priori* weighting by facet abundance. Further, instead of encoding Wulff-derived facet abundances into AEDs, we use them as a qualitative reference to assess the likelihood of facet exposure on nanoparticle catalysts and to contextualize facet-specific activity trends.

Finally, we address the estimation of product selectivity by projecting statistical moments of multi-adsorbate, facet-resolved AEDs onto a low-dimensional latent space using principal component analysis (PCA).²⁷ The resulting latent representations are used to examine how

variations in adsorption energetics across facets relate to trends in catalytic activity and product selectivity within an interpretable, data-driven framework. Together, the facet-resolved AED and latent-space analysis framework provides a statistically grounded approach to compare catalyst surfaces beyond simplified models and to identify composition–facet combinations for targeted experimental investigation in CO₂ hydrogenation.

Computational Methods

We adopted and extended the MLFF-accelerated catalyst screening framework developed in our previous work.²¹ Below, we outline the core workflow for constructing AEDs and elucidate the methodological extensions introduced in this study, including facet-resolved AED analysis, Wulff-based facet abundance estimation, and statistical analysis of AEDs. An overview of the complete workflow is shown in Figure 1.

Defining Material Space and Preparing Bulk

We studied experimentally relevant metallic catalysts primarily composed of transition metals. Our material space is comprised of the same set of elements as in our previous study: {K, V, Mn, Fe, Co, Ni, Cu, Zn, Ga, Y, Ru, Rh, Pd, Ag, In, Ir, Pt, and Au}. Stable and experimentally observed crystal phases for pure metals, binary, and ternary alloys were retrieved from the Materials Project database.²⁸

We optimized bulk geometries using the RPBE functional as implemented in the Vienna Ab Initio Simulation Package (VASP).^{29–31} We set the plane-wave cutoff to 500 eV for initial relaxations and increased it to 550 eV if necessary for convergence. We sampled the Brillouin zone with a k-point spacing of 0.17 Å⁻¹, and automated all calculations using the Atomate workflow.^{32–34}

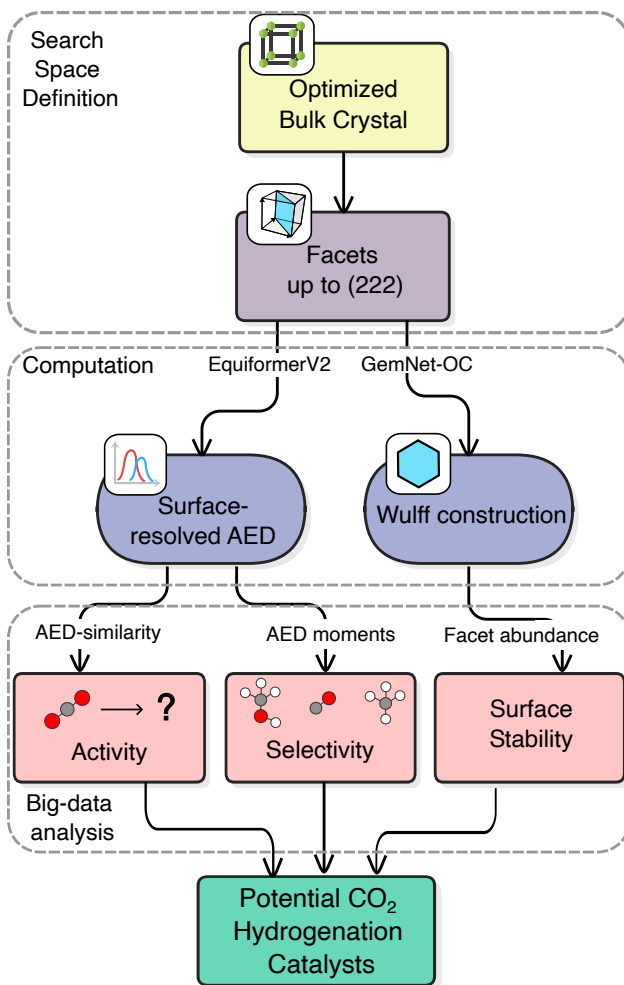


Figure 1: **Schematic overview of the ML-accelerated facet-wise catalyst screening workflow.** The workflow consists of bulk structure optimization, surface facet generation and stability filtering, preparation of adsorbate–surface configurations, MLFF-driven relaxation to local minima, adsorption energy evaluation, and subsequent data-driven analysis to gain insight into catalytic performance..

Obtaining Stable Surfaces and Wulff Construction

For each bulk material, we generated all symmetrically distinct crystallographic surfaces with Miller indices $-2 \leq h, k, l \leq 2$ using the OCP slab-generation workflow implemented in the `fairchem` toolset.^{16,35} For a given triple (hkl) , different absolute positions of the Miller plane produce different slab terminations. To narrow down the computational space, we evaluated surface energies using thicker slabs of 50 Å thickness relaxed with the total energy MLFF `gemnet-oc`.³⁶ For each Miller index, we retained only the lowest-energy termination

for subsequent AED calculations.

Further, we obtained the surface energy using the following equation:

$$\gamma = \frac{E_{\text{slab}}^{50} - NE_{\text{bulk}}}{2A} \tag{1}$$

where E_{slab}^{50} is the total MLFF-computed energy of the 50 Å slab, N is the number of slab atoms, E_{bulk} the bulk energy per atom from DFT relaxation, and A the surface area. For facets that break z -directional inversion symmetry, we relaxed both slab terminations, and the average surface energy was considered for the Wulff construction.

We determined the facet proportions in the equilibrium single crystal nanoparticle using the Wulff construction,³⁷ implemented via the `wulffpack`³⁸ package, based on our surface energy estimates.

Computing Surface-Resolved AEDs

We constructed the production slabs with a thickness of 7 Å and a vacuum spacing of 20 Å along the surface normal. We consider adsorbates *H (hydrogen atom), *CO (carbon monoxide), *OH (hydroxy), *OCHO (formate), and *OCH₃ (methoxy) crucial species during surface-bound CO₂ hydrogenation based on previous studies^{39–41} and do not follow the scaling relations.⁴² The choice of adsorbates expands our original workflow, as *CO AEDs were not part of our original study.²¹ We sampled high-symmetry adsorption sites and placed the mentioned adsorbates on the surface facets using `fairchem` tools,³⁵ then relaxed each configuration to obtain adsorption energies using the `equiformerV2` MLFF.²⁰ We calculated adsorption energies ($E_{\text{ads}}^{\text{DFT}}$) according to:

$$E_{\text{ads}}^{\text{DFT}} = E_{\text{system}}^{\text{DFT}} - E_{\text{surface}}^{\text{DFT}} - E_{\text{adsorbate}}^{\text{DFT}} \tag{2}$$

Following the convention of Chanussot et al.,¹⁶ we used linear combinations of atomic reference energies for the gas phase ($E_{\text{adsorbate}}^{\text{DFT}}$), with values of *H: -3.489 eV, *OH: -10.690

eV, *CO: -14.483 eV, *OCH3: -24.950 eV, *OCHO: -25.173 eV.

We identified unique optimized geometries within a tolerance of 0.1 Å in each spatial direction to avoid over-representation of identical local minima. In contrast to material-specific AEDs in the previous workflow,²¹ we obtained surface-resolved AEDs by aggregating the adsorption energies per Miller surface and adsorbate into a probability distribution with a 0.1 eV grid. For materials with asymmetric terminations, we aggregated adsorption energies to obtain a unified AED that represents both terminations for each Miller index. We arranged the distributions in a 1D array with sufficient separation of AEDs {-15.0, -14.9, ..., 5.0} eV to ensure sufficient decoupling between different adsorbates.

To validate the MLFF predictions, we selected three configurations for each material-adsorbate pair corresponding to the mean, median, and maximum adsorption energy and performed single-point DFT calculations on these structures and the corresponding MLFF-optimized facets with a plane-wave cutoff of 450 eV. The estimated mean absolute error (EMAE) of the MLFF predictions for each material-adsorbate pair was computed as:

$$\text{EMAE} = \frac{1}{n} \sum_{i=1}^n |E_{\text{ads},i}^{\text{DFT}} - E_{\text{ads},i}^{\text{eq2}}|, \quad (3)$$

where $n = 3$ corresponds to the three selected configurations (minimum, median, maximum) and $E_{\text{ads},i}^{\text{eq2}}$ denotes the adsorption energy predicted by the MLFF for the i^{th} configuration. Similarly to our previous work, we discarded from our analysis materials with EMAE above 0.25 eV.²¹

Modeling the Reference Catalyst

We selected a Cu-Zn catalyst as a reference system due to its well-characterized experimental performance for CO₂ hydrogenation to methanol by Behrens et al. (2012)⁴³ and Amann et al. (2022),⁴⁰ with both studies providing detailed insight into Cu(211) surfaces with substituted Zn atoms. To simulate the Cu-Zn system in the same framework as the rest of our workflow,

we built the Cu(211) system using optimized Cu(fcc) bulk and the `fairchem` workflow. To ensure sufficient separation between periodic images of the adsorbates, we constructed a 6×2 supercell of the (211) slab, in which every third atom along the upper step edge of the surface was substituted with Zn atoms. The procedure yielded a total of four Zn atoms on the 192-atom Cu(211) slab as shown in Figure 2(a) and (b). We refer to this system as Zn@Cu(211). High-symmetry adsorption sites identified via the `fairchem` workflow are also highlighted in Figure 2. The AED descriptor for this particular system is represented in Figure 2(c).

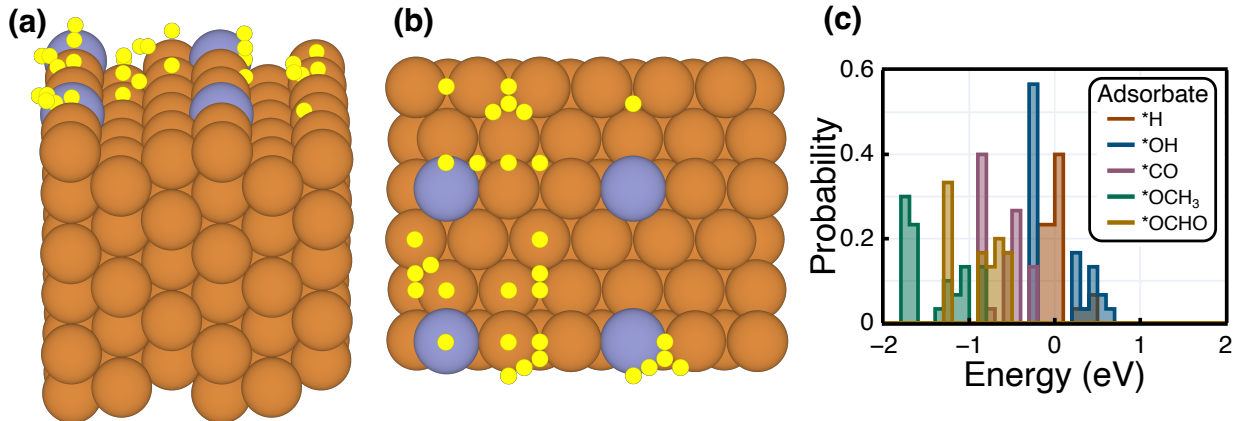


Figure 2: (a) Side view and (b) top view of the Zn@Cu(211) reference facet. Orange spheres indicate Cu atoms, purple spheres represent Zn atoms, and yellow points denote high-symmetry adsorption sites identified by the sampling algorithm. (c) AEDs for the Zn@Cu(211) facet, capturing the adsorption energies over the highlighted adsorption sites.

AED Similarity and Projection

As in our previous study, we used the Wasserstein distance metric (l_1)^{44,45} to compute similarity between facet-resolved AEDs. To obtain a compact and a more interpretable representation of the AED space, we computed statistical moments for each facet–adsorbate pair, such as the mean, median, standard deviation (std), 5th percentile (p5), minimum (min), and maximum (max). Further, we projected these AED moments onto a lower-dimensional latent space using principal component analysis (PCA). Using moments allows

us to identify which statistical features of the distributions contribute most to the observed variation across facets.

Results

Dataset and Surface-Resolved AEDs

We computed 226 stable experimentally observed materials retrieved from the Materials Project Database, spanning pure metal, binary alloy, and ternary alloy crystal phases. The complete list of bulk systems is provided in Table S1 of the Supporting Information (SI). These materials yielded 4,841 unique slab terminations, which correspond to 2,613 crystallographically distinct Miller planes. Placing the five adsorbates on the surface slabs via `fairchem` yielded approximately 1.4 million surface-adsorbate configurations, which we relaxed using `EquiformerV2` MLFF trained on the OC20 dataset with reported accuracy of 0.23 eV for adsorption energy predictions.²⁰

We validated MLFF-predicted adsorption energies through the min-max-median sampling technique described above. Across all material-adsorbate pairs, the resulting EMAE was 0.11 eV, which falls below the reported accuracy of the pretrained model. The prediction plot and the distribution of EMAE across the material space can be found in the SI (Figure S1).

The aggregated AED for Zn@Cu(211) is shown in Figure 2(c), while 12 example material facets are visualized in Figure S2 in the SI. In contrast to the broad, continuous distributions observed in material-aggregated AEDs,²¹ these facet-resolved profiles are characterized by discrete, discontinuous peaks. Qualitative inspection of facet-resolved AEDs indicates that *OCH₃ generally occupies the lowest adsorption energies among the considered intermediates on most surfaces, whereas *OH and *H often exhibit positive adsorption energies. By contrast, *OH and *H adsorption energies are often positive, and their relative position is highly material and facet-dependent. Please note that positive values do not necessarily

imply desorption, as our calculations neglect entropy, zero-point corrections, or pressure contributions. Overall, the relative ordering and spread of adsorption energies across adsorbates vary strongly between facets, indicating that simple universal trends are not easily established from single-value descriptors. Notably, *CO adsorption energies exhibit a strong dependence on the material, ranging from values near the center of the overall distribution to some of the lowest adsorption energies.

Facet-wise Comparison and Facet Stability

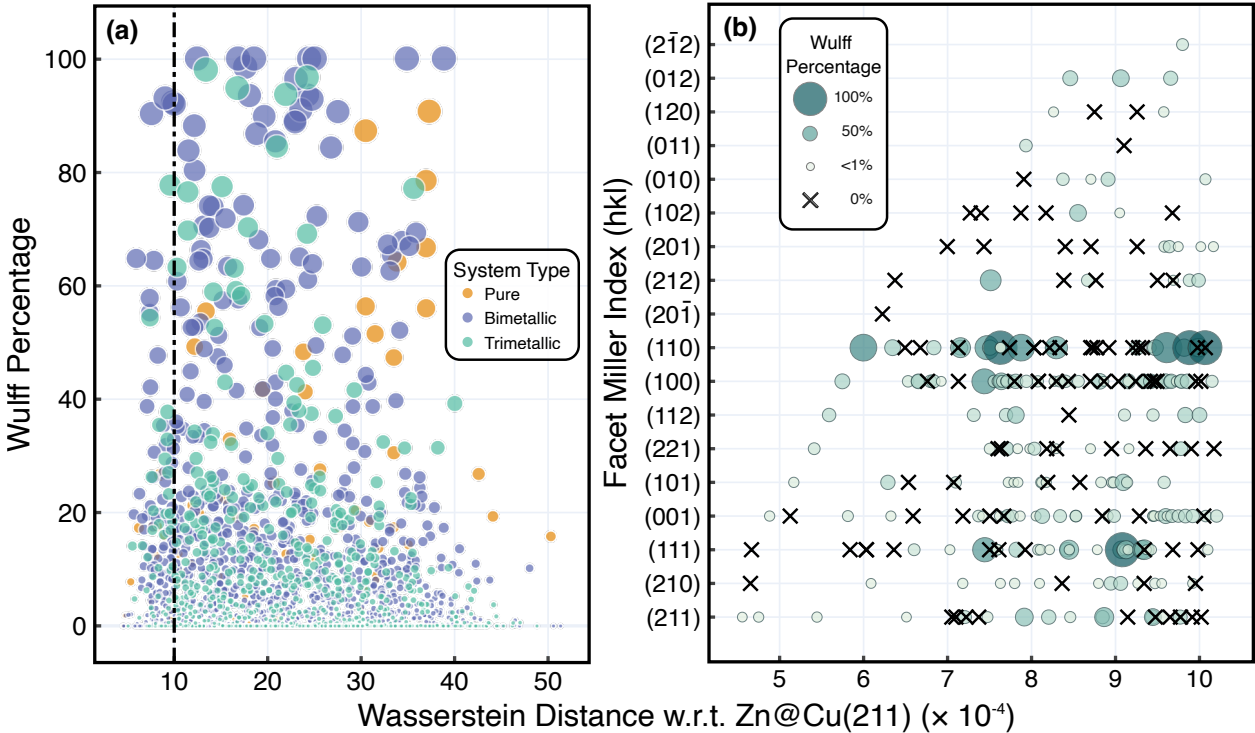


Figure 3: (a) Scatter plot of Wasserstein distance to the Zn@Cu(211) reference facet versus Wulff percentage for all catalyst facets. Marker size reflects the Wulff percentage abundance. The vertical dotted line at $l_1 = 0.001$ marks the cutoff for the top 300 facets. (b) Facet-wise AEDs across 300 catalyst facets closest to the reference AED, with marker size denoting Wulff percentage. Cross markers (\times) represent facets that are not part of the equilibrium Wulff shape in vacuum.

To compare all catalyst facets, we computed the first Wasserstein distance (l_1) between each facet and the Zn@Cu(211) reference. Figure 3(a) presents a scatter plot of the Wasserstein distance versus Wulff percentage abundance for all 2,613 distinct facets. Each facet is

colored according to its system type: pure metal, binary alloy, or ternary alloy. The size of the marker indicates the Wulff percentage, revealing that most of the facets represent less than 20% of the nanoparticle according to Wulff construction. A significant number of facets (982) exhibit zero abundance in the Wulff morphology, and as abundance increases, the number of contributing facets reduces considerably.

To focus on the material facets which are highly active, we demarcate the top 300 facets with a Wasserstein distance cutoff at $l_1 = 0.001$ for further analysis and denote them “active” facets. Within this subset, binary alloy facets predominate, followed by ternary alloys and, more rarely, pure metals. Figure 3(b) shows the facet-wise distribution of Wasserstein distances across these top facets, with the Miller indices indicated on the y -axis.

Among the top 300 facets, the most commonly observed Miller index is (110), followed by (100). Two of the closest facets, corresponding to Ag and Ru, also lie in the (211) Miller plane; however, their Wulff abundances are only 0.12% and 1.82%, respectively.. Most of the 20 facets with Wasserstein distances closest to the reference either have very low (<1%) or zero Wulff abundance. The most abundant facet among the top-300 set is $\text{In}_4\text{Ag}_9(111)$, which accounts for 64.8% of the Wulff shape. The overall distribution emphasizes low-index facets, with a limited number of facets featuring negative Miller indices.

AED Projection on 2D PCA Space

To gain deeper insight into the information encoded in AEDs, we performed PCA on the six statistical moments. PCA revealed that the first principal component (PC1) accounts for 77.29% of the explained variance (0.7728), while the second principal component (PC2) captures 8.49% (0.0849), overall summing to 85.78% variance across the dataset. The complete dataset of statistical moments and PCA coordinates have been provided on the Zenodo platform (DOI:10.5281/zenodo.20083691).

Figure 4(a) illustrates the 2D projection of the dataset including the top 10 loading vectors. Note that these vectors have been scaled for visibility and do not represent absolute

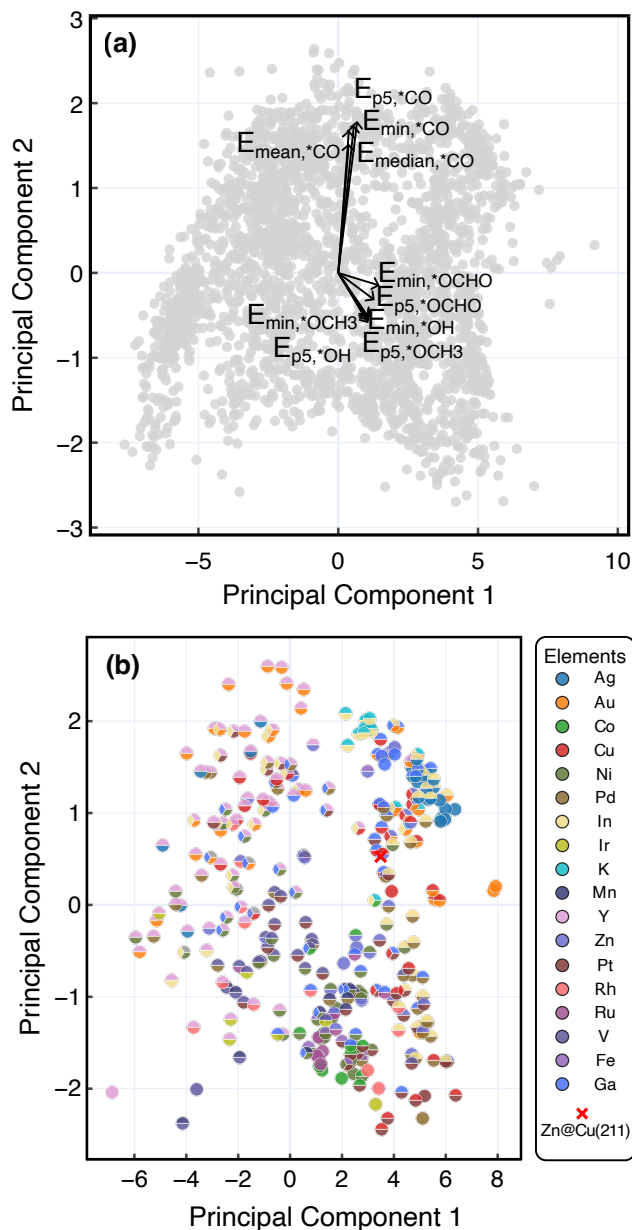


Figure 4: (a) PCA biplot showing the directionality and contribution of AED moments to each principal component. The gray datapoints represent the full AED space of the 2626 facets. Note that the loading vectors have been scaled for visibility and do not represent absolute magnitudes. (b) Two-component PCA scatter plot of the top 300 candidate facets. Each marker is a pie chart whose colored segments denote the constituent elements in the facet. The red x highlights the Zn@Cu(211) reference facet.

magnitudes. Along the PC1 direction, the loading vectors are dominated by the minimum and p_5 moments of oxygen-based adsorbates, specifically $*\text{OCH}_3$, $*\text{OCHO}$, and $*\text{OH}$. In contrast, the $*\text{CO}$ vectors exhibit the largest absolute magnitude and are oriented along the

PC2 direction. This alignment is orthogonal to the O-based adsorbates, indicating that *CO adsorption trends are uncorrelated with the oxygenate binding energies in this projection.

Figure 4(b) shows the top PCA space for the 300 facets with the lowest Wasserstein distance (l_1) to the reference facet of Zn@Cu(211) that is marked by a red “×”. In the immediate proximity of the reference, we identify a cluster of 13 binary alloy facets that have been summarized in Table 1. The list of the 300 materials-facets pairs along with their PCA space coordinates can be found in the SI (Table S3).

Table 1: Alloy facets in proximity to the reference in AED space.

Material	Facet (hkl)	Surface Fraction (%)
CuZn	(221)	0.57
Cu ₃ Ga	(110)	0.00
Ga ₂ Cu	(111)	0.73
In ₃ Ni ₂	(001)	13.00
Ga ₇ Pt ₃	(110)	0.00
ZnPd	(110)	0.00
In ₂ Pt	(211)	0.00
Cu	(221)	0.00
CuAu	(110)	0.00
In ₃ Pd ₂	(110)	0.00
Zn ₂ CuAu	(001)	0.00
YInCu ₄	(110)	26.2
K(InAu ₂) ₂	(112)	0.00

Notably, the region surrounding the reference is not uniformly populated but instead exhibits two low-density regions in the PCA latent space (Figure 4(a)). These voids correspond to combinations of significantly lower or higher O-based adsorption energetics at similar *CO binding energies relative to the reference, suggesting that such combinations are less frequently realized among the screened facets.

Moving along the direction of PC2 which aligns with increasing *CO adsorption energy; the distribution shifts toward Ag- and Ga-based materials, with additional K(InAu₂)₂ facets grouping together with KIn₄ and YAu₃ at the top of the plot. The second and third quadrants are primarily populated by Y-based material facets, with V-based facets specifically

concentrated in the third quadrant. The fourth quadrant contains facets of NiZn, Ni-Ga alloys, Co alloys, and Ru alloys. Finally, further extending in the positive PC2 direction, we observe Rh-based materials, including InRh and pure Rh.

Discussion

Surface stability and AED-based activity

In this study, we performed facet-wise screening of catalytic candidates using AEDs of relevant reaction intermediates as descriptors. In contrast to our previous facet-averaged workflow, which aggregated adsorption energetics over multiple thermodynamically stable low-index surfaces,²¹ we now resolve and analyze each crystallographic facet individually and quantify its apparent catalytic activity based on the similarity of its AED to that of the Zn@Cu(211) reference facet. Specifically, we use the first Wasserstein distance between facet-resolved AEDs as a measure of proximity in adsorption energy space, such that facets with smaller Wasserstein distance to Zn@Cu(211) are considered more likely to reproduce its adsorption landscape associated with methanol formation.

Beyond providing a structural fingerprint, AEDs enable a quantitative comparison of apparent facet activity across a diverse material space. The fingerprint aids us to identify facets that are drastically different from the reference yet possess very similar AED fingerprints (top 300 facets are provided in the SI Table S3) and subsequently the activity toward CO₂ hydrogenation.

A recurring observation in our screening is that facets with similar AED fingerprints to the reference Zn@Cu(211) often exhibit low or zero theoretical abundance in the equilibrium Wulff construction (Fig. 3). While this initially suggests that these facets are less stable, it is crucial to recognize that the Wulff model approximates an isolated nanocrystal in vacuum. In practice, kinetics, support effects, synthesis conditions (e.g., temperature, precursors), and reaction environments can drastically alter surface energies, stabilizing facets

that would otherwise be transient.^{46,47} The prevalence of low-abundance facets in proximity to the reference highlights the potential need for tailored synthesis protocols designed to kinetically trap these specific terminations. Our analysis therefore reveals that the facets whose adsorption landscapes most closely resemble the active Zn@Cu(211) reference tend to be thermodynamically disfavored in the vacuum Wulff construction, yet may be stabilized under realistic synthesis and reaction conditions.

Limitations of Wasserstein distance similarity measure

Our analysis highlights both the utility and limitations of the Wasserstein distance (l_1) as a similarity metric for screening catalysts, suggested in our previous study.²¹ While l_1 effectively ranks overall similarity in distribution shape, it provides only a coarse measure of absolute shifts in adsorption energies when distributions retain similar shapes. As a result, facets with systematically stronger or weaker binding across all sites may still appear close, if their AEDs are shape-preserving shifts. This necessitates a multimodal approach such as the moment-based PCA that combines additional information from the AEDs to fully resolve the catalytic fingerprint of a surface.

Furthermore, as for any reference-based screening, the choice of the Zn@Cu(211) facet inherently influences the screening outcomes. The preponderance of binary alloys in the “active” category may reflect a bias in the l_1 metric towards compositions that stoichiometrically resemble the reference. This observation suggests that while our current candidates are promising, future experimentation should incorporate ternary alloy benchmarks to fully explore the advantages of higher-order compositional complexity.

Selectivity of Facets

With the principal component analysis of the AED moments we reduce the dimensionality of our descriptor space and provide a physically interpretable map of selectivity trends in the dataset. As shown in Figure 4(a), PC1 is dominated by moments of oxygenated intermediates

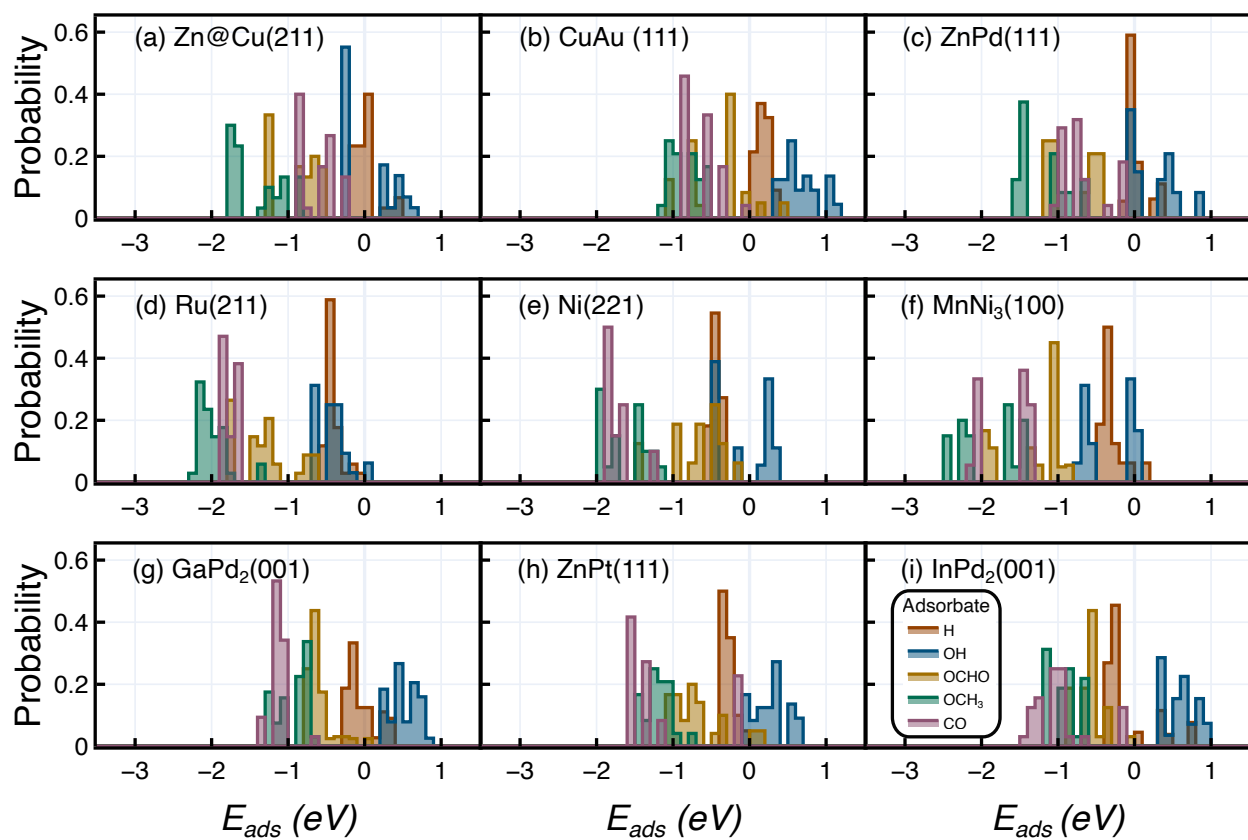


Figure 5: (a–i) AEDs for the 9 catalyst facets identified as close to the Zn@Cu(211) reference determined by Wasserstein distance analysis.

(*OCH₃, *OCHO, *OH), whereas PC2 is primarily governed by *CO-related moments. This structure allows us to view the AED–PCA map as a two-dimensional analogue of a volcano plot, where the PC1 axis reflects variations in oxygenate binding strength and the PC2 axis captures systematic changes in *CO binding. In this representation, facets occupy distinct regions associated with different combinations of oxygenate and *CO adsorption energies, which can be related to C1 product selectivity using literature-based trends.

We illustrate these trends by organizing AEDs of 9 example facets in Figure 5 into three rows. For the facets in the top row (Fig. 5(a–c)), *CO binding energies range between -1 and 0 eV. However, for other candidates (Fig. 5(d–i)), *CO binds significantly stronger (< -1 eV down to -2 eV), a trend that spatially correlates with their location in the fourth quadrant of the PCA space. Notably, CuAu(111) and ZnPd(111) (top row) exhibit the highest proximity to the Zn@Cu(211) reference in both l_1 distance and PCA projection, identifying them as the most promising candidates for replicating the reference’s catalytic performance toward CO₂-to-methanol conversion.

To connect this information with catalytic behaviour, we performed a literature search for adsorption energies of oxygenated species and *CO on different materials: The optimal *OCH₃ binding, close to the reference, favors the methanol pathway. Deviations in the first PC axis, particularly towards weaker oxygenate binding, point to alternative products. For instance, candidates (g) through (i) in Figure 5 exhibit *OCHO energies between -1 and 0 eV (weaker than the reference); this specific destabilization of the formate intermediate suggests a preference for less hydrogenated products, such as formic acid or formaldehyde, over methanol.⁴⁸

Similarly, higher *CO adsorption energies (top-right PCA region) imply facile desorption, potentially preventing further hydrogenation and favoring CO production.²² For instance, In–Ag alloys and other Ag-based materials, are known for their low CO₂ conversion efficiency and high selectivity toward the Reverse Water-Gas Shift (RWGS) reaction.^{49–51}

Moving lower along the *CO loading vector (PC2) reveals strong-binding candidates like

Ru(221) and Ni(221). Ru, Ni, and Co-based facets in this quadrant have a proven tendency to retain CO on the surface for complete hydrogenation to methane.^{52–56}

The Zn@Cu(211) reference lies in an intermediate *CO-binding region (approx. -1 to 0 eV), suggesting that selective methanol synthesis requires moderate *CO binding strong enough for activation but weak enough to avoid over-hydrogenation to methane or surface poisoning. Table 2 summarizes the anticipated major products for the top candidates, based on their l_1 closeness and positions in the PCA selectivity map. Notably, candidates within the “methanol window” are supported by experimental literature; for instance, CuAu nanoalloys have been shown to enhance CO₂ reduction to CH₃OH.⁵⁷ While our specific top-ranked CuAu(111) facet shows low Wulff abundance, other CuAu facets map to the same favorable region in PCA space, suggesting that the catalytic effect is robust across multiple surface terminations. Similarly, the identification of ZnPd(111) 5(c) aligns with studies demonstrating methanol selectivity in Zn-Pd systems.⁵⁸

While both PC axes seem to affect the selectivity of facets and materials, the *CO axis serves as a critical determinant for C1 product distribution. Although the boundaries between methanol, methane, and other C1 products are not perfectly sharp, the clustering of these known materials validates the prediction capability of the AED-PCA map and thus establishes this descriptor as a robust foundation for catalyst discovery. The expected C1 product selectivity based on the PCA map of AED moments for the 30 closest facets to the reference is shown in Table 2.

Overall, the AED-PCA map indicates that both principal components influence C1 product selectivity, but that the *CO-dominated PC2 axis plays a particularly critical role in partitioning methanol-, methane-, and CO/RWGS-selective regions of the space. The clustering of experimentally known methanol-, methane-, and CO-selective catalysts in the corresponding regions provides retrospective support for the AED-based selectivity picture and motivates the use of facet-resolved AED moments as a physically interpretable descriptor for guiding future catalyst discovery.

Table 2: Product selectivity based on 2D PCA map.

System	Wulff %	PC1	PC2	Selectivity
Zn@Cu(211)	-	3.54	0.51	CH ₃ OH
Ag(211)	0.01	5.84	0.95	CO
InAg ₃ (210)	0.00	5.29	1.14	CO
CuAu(111)	0.00	5.58	0.06	CH ₃ OH
Ru(211)	1.82	1.26	-1.59	CH ₄
GaPd ₂ (001)	1.85	4.91	-1.13	HCOOH
K(InAu ₂) ₂ (001)	0.00	4.92	1.64	CO
YAu(101)	1.97	-5.79	-0.51	-
Ni(221)	7.79	2.46	-1.84	CH ₄
KIn ₄ (211)	2.06	2.63	1.86	CO?
Y ₂ GaNi ₂ (112)	14.10	-2.62	-0.28	-
MnNi ₃ (100)	19.67	1.18	-1.46	CH ₄
YGaRh(001)	4.77	-1.89	-0.02	-
ZnPd(111)	0.00	3.81	-0.02	CH ₃ OH
In ₄ Ag ₉ (110)	64.77	5.53	1.27	CO
Ni ₂ Zn ₂ (111)	0.00	2.63	-0.94	CH ₄
YIn(111)	0.00	-3.23	-0.49	-
YAu ₃ (210)	0.44	-2.90	1.92	-
Ni ₁₃ Ga ₉ (20 $\bar{1}$)	0.00	1.78	-1.13	CH ₄
Ag(101)	17.29	6.35	1.04	CO
YInPt(001)	1.45	-2.16	1.89	-
Y ₃ Pd ₄ (110)	23.31	-0.48	1.26	-
ZnPt(111)	0.00	3.96	-1.04	HCOOH
Zn ₂ (212)	0.00	2.56	-0.46	CO?
KAu ₅ (110)	0.00	4.96	1.04	CO
Co ₂ (211)	0.01	1.23	-1.80	CH ₄
YAu(100)	6.73	-2.69	0.81	-
YAu ₂ (101)	0.00	-3.99	1.65	-
InPd ₂ (001)	0.00	5.11	-1.00	HCOOH
YIr ₂ (111)	8.12	-2.29	-1.25	-
ZrZnCu ₂ (100)	14.16	0.50	0.54	CH ₃ OH
Ni ₃ Pt(100)	18.97	3.15	-1.58	CH ₄

Conclusions

In this work, we used MLFF-driven high-throughput simulations to construct facet-resolved AEDs for metallic, binary, and ternary alloy catalysts for thermal CO₂ hydrogenation. Transitioning from single-site descriptors to distributions, our analysis shows that AEDs contain information on both activity and selectivity. Similarity in AED space to a well-performing reference facet provides a practical proxy for apparent activity, while projection of AED moments onto a low-dimensional latent space reveals systematic trends in C1 product selectivity across different facets and alloy compositions. The resulting workflow yields a prioritized list of composition–facet combinations for experimental validation in CO₂ hydrogenation, with particular focus on methanol production. The analysis also unravels promising material-facet combinations toward other C1 products. Our framework is readily transferable to other reactions and material classes, and paves the way to integrating MLFF-based high-throughput screening with interpretable, distribution-based descriptors in catalyst discovery.

Acknowledgement

The authors would like to thank Annukka Santasalo-Aarnio and Arpad Toldy for fruitful discussions. O.K. and P.P. express their gratitude to Kirby Broderick, Adeesh Koluru, Brook Wander, John Kitchin, and other Kitchin Research Group members at Carnegie Mellon University, as well as Zachary Ulissi at Meta, for their assistance with the OCP models. This project received funding from the Deutsche Forschungsgemeinschaft (DFG, German Research Foundation) under Germany’s Excellence Strategy – EXC 2089/2 – 390776260, and the European Union – NextGenerationEU instrument from the Research Council of Finland’s AIcon project (grant number 348179). O.K. was supported by the Research Council of Finland under project number 371666. The authors further gratefully acknowledge CSC – IT Center for Science, Finland, and the Aalto Science-IT project for generous computational resources.

The authors used LLM tools to strengthen the language of this manuscript. The authors reviewed and edited the content and take full responsibility for the content of the publication.

Data Availability

All data are available at Zenodo, DOI: 10.5281/zenodo.20083691.

Supporting Information Available

All 226 materials used in the final evaluation; Materials removed from the final evaluation; Statistics on adsorption energy prediction (a) prediction plot (b) distribution of estimated mean absolute error across materials AEDs for top 12 facets closest to the reference Zn@Cu(211) 300 closest surface orientations w.r.t. Wasserstein distance of AEDs to the reference AED (Zn@Cu(211)) (in ascending order) along with their Wulff percentages and coordinates in the 2D latent PCA space of the AED moments.

References

- (1) Hu, B.; Guild, C.; Suib, S. L. Thermal, electrochemical, and photochemical conversion of CO₂ to fuels and value-added products. *Journal of CO₂ Utilization* **2013**, *1*, 18–27.
- (2) Ye, R.-P.; Ding, J.; Gong, W.; Argyle, M. D.; Zhong, Q.; Wang, Y.; Russell, C. K.; Xu, Z.; Russell, A. G.; Li, Q.; Fan, M.; Yao, Y.-G. CO₂ hydrogenation to high-value products via heterogeneous catalysis. *Nature Communications* **2019**, *10*.
- (3) Zhang, M.; Wang, M.; Xu, B.; Ma, D. How to Measure the Reaction Performance of Heterogeneous Catalytic Reactions Reliably. *Joule* **2019**, *3*, 2876–2883.
- (4) Beck, A.; Newton, M. A.; Water, L. G. A. v. d.; Bokhoven, J. A. v. The Enigma

- of Methanol Synthesis by Cu/ZnO/Al₂O₃-Based Catalysts. *Chemical Reviews* **2024**, Publisher: American Chemical Society.
- (5) Ye, J.; Dimitratos, N.; Rossi, L. M.; Thonemann, N.; Beale, A. M.; Wojcieszak, R. Hydrogenation of CO₂ for sustainable fuel and chemical production. *Science* **2025**, *387*, eadn9388, Publisher: American Association for the Advancement of Science.
- (6) Bahri, S.; Pathak, S.; Singhluwalia, A.; Malav, P.; Upadhyayula, S. Meta-analysis approach for understanding the characteristics of CO₂ reduction catalysts for renewable fuel production. *Journal of Cleaner Production* **2022**, *339*, 130653.
- (7) Zada, H.; Yu, J.; Fang, C.; Jian Sun Disentangling the activity-selectivity trade-off in CO₂ hydrogenation to methanol. *Chem* **2026**, 102942.
- (8) Benavides-Hernández, J.; Dumeignil, F. From Characterization to Discovery: Artificial Intelligence, Machine Learning and High-Throughput Experiments for Heterogeneous Catalyst Design. *ACS Catalysis* **2024**, *14*, 11749–11779.
- (9) Ortega, C.; Otyuskaya, D.; Ras, E.; Virla, L. D.; Patience, G. S.; Dathe, H. Experimental methods in chemical engineering: High throughput catalyst testing — HTCT. *The Canadian Journal of Chemical Engineering* **2021**, *99*, 1288–1306.
- (10) Dongapure, P.; Tekawadia, J.; Thundiyil, S.; Caha, I.; Deepak, F. L.; Devi, R. N. Mechanistic Insights into Near Ambient Pressure Activity of Intermetallic NiZn/TiO₂ Catalyst for CO₂ Conversion to Methanol. *ChemCatChem* **2023**, *15*, e202201150, eprint: <https://onlinelibrary.wiley.com/doi/pdf/10.1002/cctc.202201150>.
- (11) Medford, A. J.; Vojvodic, A.; Hummelshøj, J. S.; Voss, J.; Abild-Pedersen, F.; Studt, F.; Bligaard, T.; Nilsson, A.; Nørskov, J. K. From the Sabatier principle to a predictive theory of transition-metal heterogeneous catalysis. *Journal of Catalysis* **2015**, *328*, 36–42.

- (12) Nørskov, J. K.; Abild-Pedersen, F.; Studt, F.; Bligaard, T. Density functional theory in surface chemistry and catalysis. *Proceedings of the National Academy of Sciences* **2011**, *108*, 937–943.
- (13) Jones, G.; Bligaard, T.; Abild-Pedersen, F.; Nørskov, J. K. Using scaling relations to understand trends in the catalytic activity of transition metals. *Journal of Physics: Condensed Matter* **2008**, *20*, 064239.
- (14) Feng, Y.; Chen, Y.; Zheng, L.; Chen, X.; Li, T.; Zhao, W. Descriptors construction and application in catalytic site design. *iScience* **2025**, *28*.
- (15) Ouyang, R.; Curtarolo, S.; Ahmetcik, E.; Scheffler, M.; Ghiringhelli, L. M. SISSO: A compressed-sensing method for identifying the best low-dimensional descriptor in an immensity of offered candidates. *Physical Review Materials* **2018**, *2*, 083802.
- (16) Chanussot, L. et al. Open Catalyst 2020 (OC20) Dataset and Community Challenges. *ACS Catalysis* **2021**, *11*, 6059–6072.
- (17) Kang, P.-L.; Shang, C.; Liu, Z.-P. Large-Scale Atomic Simulation via Machine Learning Potentials Constructed by Global Potential Energy Surface Exploration. *Accounts of Chemical Research* **2020**, *53*, 2119–2129.
- (18) Tran, R. et al. The Open Catalyst 2022 (OC22) Dataset and Challenges for Oxide Electrocatalysts. *ACS Catal.* **2023**, *13*, 3066–3084.
- (19) Kim, J. et al. Accelerated discovery of CO₂-to-C₃-hydrocarbon electrocatalysts with human-in-the-loop. *Joule* **2025**, *0*, Publisher: Elsevier.
- (20) Liao, Y.-L.; Wood, B.; Das, A.; Smidt, T. EquiformerV2: Improved Equivariant Transformer for Scaling to Higher-Degree Representations. *arXiv preprint arXiv:2306.12059* **2023**, Published as a conference paper at ICLR 2024.

- (21) Pisal, P.; Krejčí, O.; Rinke, P. Machine learning accelerated descriptor design for catalyst discovery in CO₂ to methanol conversion. *npj Computational Materials* **2025**, *11*.
- (22) Ye, R.; Ding, J.; Reina, T. R.; Duyar, M. S.; Li, H.; Luo, W.; Zhang, R.; Fan, M.; Feng, G.; Sun, J.; Liu, J. Design of catalysts for selective CO₂ hydrogenation. *Nature Synthesis* **2025**, *4*, 288–302, Publisher: Nature Publishing Group.
- (23) Wang, Q.; Yao, Y. Harnessing machine learning for high-entropy alloy catalysis: a focus on adsorption energy prediction. *npj Computational Materials* **2025**, *11*, 91, Publisher: Nature Publishing Group.
- (24) Pedersen, J. K.; Batchelor, T. A. A.; Bagger, A.; Rossmeisl, J. High-Entropy Alloys as Catalysts for the CO₂ and CO Reduction Reactions. *ACS Catalysis* **2020**, *10*, 2169–2176.
- (25) Tang, M. T.; Peng, H.; Lamoureux, P. S.; Bajdich, M.; Abild-Pedersen, F. From electricity to fuels: Descriptors for C1 selectivity in electrochemical CO₂ reduction. *Applied Catalysis B: Environmental* **2020**, *279*, 119384.
- (26) Mok, D. H.; Li, H.; Zhang, G.; Lee, C.; Jiang, K.; Back, S. Data-driven discovery of electrocatalysts for CO₂ reduction using active motifs-based machine learning. *Nature Communications* **2023**, *14*, 7303, Publisher: Nature Publishing Group.
- (27) Maćkiewicz, A.; Ratajczak, W. Principal components analysis (PCA). *Computers & Geosciences* **1993**, *19*, 303–342.
- (28) Jain, A.; Ong, S. P.; Hautier, G.; Chen, W.; Richards, W. D.; Dacek, S.; Cholia, S.; Gunter, D.; Skinner, D.; Ceder, G.; Persson, K. A. Commentary: The Materials Project: A materials genome approach to accelerating materials innovation. *APL Materials* **2013**, *1*, 011002.

- (29) Hammer, B.; Hansen, L. B.; Nørskov, J. K. Improved adsorption energetics within density-functional theory using revised Perdew-Burke-Ernzerhof functionals. *Phys. Rev. B* **1999**, *59*, 7413–7421.
- (30) Kresse, G.; Hafner, J. Ab initio molecular-dynamics simulation of the liquid-metal–amorphous-semiconductor transition in germanium. *Phys. Rev. B* **1994**, *49*, 14251–14269.
- (31) Kresse, G.; Furthmüller, J. Efficient iterative schemes for ab initio total-energy calculations using a plane-wave basis set. *Phys. Rev. B* **1996**, *54*, 11169–11186.
- (32) Mathew, K. et al. Atomate: A high-level interface to generate, execute, and analyze computational materials science workflows. *Computational Materials Science* **2017**, *139*, 140–152.
- (33) Jain, A.; Ong, S. P.; Chen, W.; Medasani, B.; Qu, X.; Kocher, M.; Brafman, M.; Petretto, G.; Rignanese, G.-M.; Hautier, G.; Gunter, D.; Persson, K. A. FireWorks: a dynamic workflow system designed for high-throughput applications. *Concurrency and Computation: Practice and Experience* **2015**, *27*, 5037–5059.
- (34) Ong, S. P.; Richards, W. D.; Jain, A.; Hautier, G.; Kocher, M.; Cholia, S.; Gunter, D.; Chevrier, V. L.; Persson, K. A.; Ceder, G. Python Materials Genomics (pymatgen): A robust, open-source python library for materials analysis. *Computational Materials Science* **2013**, *68*, 314–319.
- (35) FAIR-Chem fairchem: A FAIR-Chem Project Repository. 2024; <https://github.com/FAIR-Chem/fairchem>.
- (36) Gasteiger, J.; Shuaibi, M.; Sriram, A.; Günnemann, S.; Ulissi, Z.; Zitnick, C. L.; Das, A. GemNet-OC: Developing Graph Neural Networks for Large and Diverse Molecular Simulation Datasets. 2022; <http://arxiv.org/abs/2204.02782>, arXiv:2204.02782 [cond-mat, physics:physics].

- (37) Ringe, E.; Van Duyne, R. P.; Marks, L. D. Wulff Construction for Alloy Nanoparticles. *Nano Letters* **2011**, *11*, 3399–3403, Publisher: American Chemical Society.
- (38) Rahm, J. M.; Erhart, P. WulffPack: A Python package for Wulff constructions. *Journal of Open Source Software* **2020**, *5*, 1944.
- (39) Tang, A.; Wu, G.; Chai, Y.; Li, L. CO₂ Selective Hydrogenation to Methanol Catalyzed by CuZn Active Sites Confined in Silicalite-1 Zeolite. *ACS Catalysis* **2025**, 19984–19993.
- (40) Amann, P. et al. The state of zinc in methanol synthesis over a Zn/ZnO/Cu(211) model catalyst. *Science* **2022**, *376*, 603–608.
- (41) Zimmerli, N. K.; Usuga, A. F.; Checchia, S.; Comas-Vives, A.; Müller, C. R.; Abdala, P. M. How Does the Ni–Ga Alloy Structure Tune Methanol Productivity and Selectivity? *ACS Catalysis* **2025**, *15*, 14252–14266.
- (42) Montemore, M. M.; Medlin, J. W. Scaling relations between adsorption energies for computational screening and design of catalysts. *Catalysis Science & Technology* **2014**, *4*, 3748–3761, Publisher: The Royal Society of Chemistry.
- (43) Behrens, M.; Studt, F.; Kasatkin, I.; Kühl, S.; Hävecker, M.; Abild-Pedersen, F.; Zander, S.; Girgsdies, F.; Kurr, P.; Knief, B.-L.; Tovar, M.; Fischer, R. W.; Nørskov, J. K.; Schlögl, R. The Active Site of Methanol Synthesis over Cu/ZnO/Al₂O₃ Industrial Catalysts. *Science* **2012**, *336*, 893–897, Publisher: American Association for the Advancement of Science.
- (44) Virtanen, P. et al. SciPy 1.0: Fundamental Algorithms for Scientific Computing in Python. *Nature Methods* **2020**, *17*, 261–272.
- (45) Ramdas, A.; García Trillos, N.; Cuturi, M. On Wasserstein two-sample testing and related families of nonparametric tests. *Entropy* **2017**, *19*, 47.

- (46) Ringe, E.; Van Duyne, R. P.; Marks, L. D. Kinetic and Thermodynamic Modified Wulff Constructions for Twinned Nanoparticles. *The Journal of Physical Chemistry C* **2013**, *117*, 15859–15870, Publisher: American Chemical Society.
- (47) Xing, M.; Pathak, A.-D.; Sanyal, S.; Peng, Q.; Liu, X.; Wen, X. Temperature-dependent surface free energy and the Wulff shape of iron and iron carbide nanoparticles: A molecular dynamics study. *Applied Surface Science* **2020**, *509*, 144859.
- (48) Sun, R.; Liao, Y.; Bai, S.-T.; Zheng, M.; Zhou, C.; Zhang, T.; Sels, B. F. Heterogeneous catalysts for CO₂ hydrogenation to formic acid/formate: from nanoscale to single atom. *Energy & Environmental Science* **2021**, *14*, 1247–1285.
- (49) Choi, S.; Sang, B.-I.; Hong, J.; Yoon, K. J.; Son, J.-W.; Lee, J.-H.; Kim, B.-K.; Kim, H. Catalytic behavior of metal catalysts in high-temperature RWGS reaction: In-situ FT-IR experiments and first-principles calculations. *Scientific Reports* **2017**, *7*, 41207, Publisher: Nature Publishing Group.
- (50) Zhang, C.; Zhang, R.; Liu, Y.; Wu, X.; Wang, H.; Ge, Q.; Zhu, X. Blocking Methanation during Reverse Water Gas Shift Reaction on Ni/SiO₂ Catalysts by Surface Ag. *ChemCatChem* **2023**, *15*, e202201284, eprint: <https://chemistry-europe.onlinelibrary.wiley.com/doi/pdf/10.1002/cctc.202201284>.
- (51) Barasa, G. O.; Awino, C.; Li, C.; Agumba, J. O.; Okoth, K. O.; Magero, D. Indium decorated nanoporous Ag as an efficient catalyst for enhanced CO₂ electroreduction. *Solid State Sciences* **2022**, *129*, 106916.
- (52) Guo, X.; Peng, Z.; Traitangwong, A.; Wang, G.; Xu, H.; Meeyoo, V.; Li, C.; Zhang, S. Ru nanoparticles stabilized by ionic liquids supported onto silica: highly active catalysts for low-temperature CO₂ methanation. *Green Chemistry* **2018**, *20*, 4932–4945, Publisher: The Royal Society of Chemistry.

- (53) Chai, S.; Men, Y.; Wang, J.; Liu, S.; Song, Q.; An, W.; Kolb, G. Boosting CO₂ methanation activity on Ru/TiO₂ catalysts by exposing (001) facets of anatase TiO₂. *Journal of CO₂ Utilization* **2019**, *33*, 242–252.
- (54) Musab Ahmed, S.; Ren, J.; Ullah, I.; Lou, H.; Xu, N.; Abbasi, Z.; Wang, Z. Ni-Based Catalysts for CO₂ Methanation: Exploring the Support Role in Structure-Activity Relationships. *ChemSusChem* **2024**, *17*, e202400310, eprint: <https://chemistry-europe.onlinelibrary.wiley.com/doi/pdf/10.1002/cssc.202400310>.
- (55) Evtushkova, A.; Heinrichs, J. M.; Parastaev, A.; Kosinov, N.; Hensen, E. J. M. Flame Synthesized Co–CeO₂ Catalysts for CO₂ Methanation. *ACS Catalysis* **2025**, *15*, 11217–11231.
- (56) Schubert, M.; Pokhrel, S.; Thomé, A.; Zielasek, V.; Gesing, T. M.; Roessner, F.; Mädler, L.; Bäumer, M. Highly active Co–Al₂O₃-based catalysts for CO₂ methanation with very low platinum promotion prepared by double flame spray pyrolysis. *Catalysis Science & Technology* **2016**, *6*, 7449–7460, Publisher: The Royal Society of Chemistry.
- (57) Mosrati, J.; Ishida, T.; Mac, H.; Al-Yusufi, M.; Honma, T.; Parliniska-Wojtan, M.; Kobayashi, Y.; Klyushin, A.; Murayama, T.; Abdel-Mageed, A. M. Low-Temperature Hydrogenation of CO₂ to Methanol in Water on ZnO-Supported CuAu Nanoalloys. *Angewandte Chemie International Edition* **2023**, *62*, e202311340, eprint: <https://onlinelibrary.wiley.com/doi/pdf/10.1002/anie.202311340>.
- (58) Brix, F.; Desbuis, V.; Piccolo, L.; Gaudry, E. Tuning Adsorption Energies and Reaction Pathways by Alloying: PdZn versus Pd for CO₂ Hydrogenation to Methanol. *The Journal of Physical Chemistry Letters* **2020**, *11*, 7672–7678, Publisher: American Chemical Society.

TOC Graphic

